Effect of Crystallographic Structure of MnO2 on Its Electrochemical Capacitance Properties

2 AUTHORS, INCLUDING:

DEVARAJ S

SASTRA University

17 PUBLICATIONS   781 CITATIONS

Effect of Crystallographic Structure of MnO₂ on Its Electrochemical Capacitance Properties

S. Devaraj and N. Munichandraiah*

Department of Inorganic and Physical Chemistry, Indian Institute of Science, Bangalore - 560 012, India

Received: November 14, 2007; In Final Form: January 7, 2008

MnO₂ is currently under extensive investigations for its capacitance properties. MnO₂ crystallizes into several crystallographic structures, namely, α, β, γ, δ, and λ structures. Because these structures differ in the way MnO₆ octahedra are interlinked, they possess tunnels or interlayers with gaps of different magnitudes. Because capacitance properties are due to intercalation/deintercalation of protons or cations in MnO₂, only some crystallographic structures, which possess sufficient gaps to accommodate these ions, are expected to be useful for capacitance studies. In order to examine the dependence of capacitance on crystal structure, the present study involves preparation of these various crystal phases of MnO₂ in nanodimensions and to evaluate their capacitance properties. Results of α-MnO₂ prepared by a microemulsion route (α-MnO₂(m)) are also used for comparison. Spherical particles of about 50 nm, nanorods of 30–50 nm in diameter, or interlocked fibers of 10–20 nm in diameters are formed, which depend on the crystal structure and the method of preparation. The specific capacitance (SC) measured for MnO₂ is found to depend strongly on the crystallographic structure, and it decreases in the following order: α(m) > $\alpha \cong \delta$ > γ > λ > β. A SC value of 297 F g^{-1} is obtained for α-MnO₂(m), whereas it is 9 F g^{-1} for β-MnO₂. A wide (~4.6 Å) tunnel size and large surface area of α-MnO₂(m) are ascribed as favorable factors for its high SC. A large interlayer separation (~7 Å) also facilitates insertion of cations in δ-MnO₂ resulting in a SC close to 236 F g^{-1}. A narrow tunnel size (1.89 Å) does not allow intercalation of cations into β-MnO₂. As a result, it provides a very small SC.

1. Introduction

In recent years, electrochemical capacitors (ECs) have received a great attention in the filed of electrochemical energy storage and conversion because of their high power capability and long cycle-life. An EC is useful as an auxiliary energy device along with a primary power source such as a battery or a fuel cell for power enhancement in short pulse applications.[1–4] Charge storage mechanisms in EC capacitor materials include separation of charges at the interface between the electrode and the electrolyte and/or fast faradaic reactions occurring at the electrode. Capacitance, which arises from separation of charges, is generally called electric double-layer capacitance (EDLC). Capacitance due to a faradaic process is known as pseudocapacitance. Because the magnitude of capacitance of these types of capacitors is several times greater than that of conventional capacitors, ECs are also known as supercapacitors or ultracapacitors.

Various materials investigated for ECs include (i) carbonous materials, (ii) conducting polymers, and (iii) transition-metal oxides.[3] Among transition-metal oxides, amorphous hydrous ruthenium oxide (RuO₂·xH₂O) has specific capacitance (SC) as high as 760 F g^{-1} because of the solid-state pseudofaradaic reaction.[5–8] However, the high cost, low porosity, and toxic nature of RuO₂ limit commercialization of supercapacitors employing this material. Therefore, there is a need to investigate alternate transition-metal oxides, which are cheap, available in abundance, nontoxic, and environmentally friendly. Manganese dioxide has attracted much attention[9–21] because it has these favorable properties and it is widely used as a cathode material in batteries.[22] However, the SC values reported are lower than

the values obtained for RuO₂·xH₂O, and studies on various ways of increasing the SC are reported.[14,15]

Hydrous MnO₂ exhibits pseudocapacitance behavior in several aqueous electrolytes of alkali salts such as Li₂SO₄, Na₂SO₄, K₂SO₄, and so forth. Transition of Mn^{4+}/Mn^{3+} involving a single electron transfer is responsible for the pseudocapacitance behavior of MnO₂.[10,23,24] MnO₂ exists in several crystallographic forms, which are known as α, β, γ, δ, and λ forms.[22,25] The α, β, and γ forms possess 1D tunnels in their structures, the δ is a 2D layered compound, and the λ is a 3D spinel structure. The properties of MnO₂ largely depend on its crystallographic nature. Because of various crystallographic structures, MnO₂ is useful as a molecular sieve,[26] a catalyst,[27] and an electrode material in batteries[22] as well as in supercapacitors.[9–21] Because these structures differ in the way MnO₆ octahedra are interlinked, they possess tunnels or interlayers with gaps of different magnitudes. Because capacitance properties are due to intercalation/deintercalation of protons or cations in MnO₂, only the crystallographic structures, which possess sufficient gaps to accommodate these ions, are anticipated to be useful for capacitance studies. It is expected that the amount of alkali cations or protons intercalated/extracted into/from MnO₂ lattice and hence its SC largely depends on either the size of the tunnel or the interlayer separation between sheets of MnO₆ octahedra.

MnO₂ with three different crystallographic forms (α, β, and γ) was prepared by the hydrothermal–electrochemical method, and lithium insertion behavior was studied.[28,29] α- and γ-MnO₂ were prepared by the electrolysis of aqueous MnSO₄ solution containing various alkali and alkaline earth salts at various pH and potential values. It was found that the crystallographic structure of MnO₂ depends on the radius of the alkali or alkaline earth metal-ion, the pH, and the potential.[30] Brousse et al. studied the dependence of capacitance on surface area for various

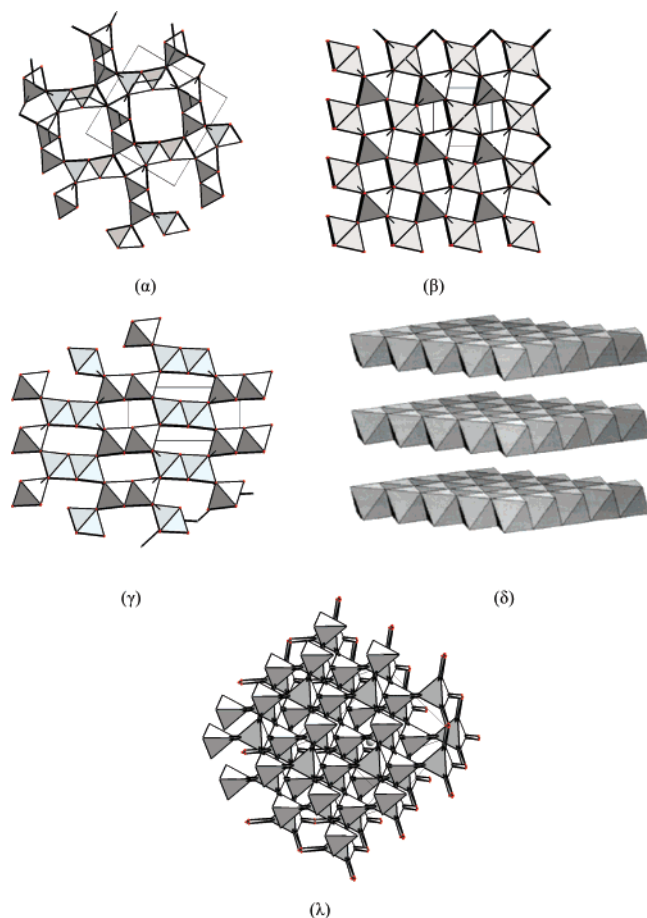* Corresponding author. Tel: +91-80-22933183. Fax: +91-80-23600683. E-mail: muni@ipc.iisc.ernet.in.

Effect of Crystallographic Structure of MnO2

J. Phys. Chem. C, Vol. 112, No. 11, 2008 **4407**

Figure 1. Crystal structures of α-, β-, γ-, δ-, and λ-MnO2.

TABLE 1: Tunnel Size of Different Crystallographic Forms of MnO2[34−36]

crystallographic form	tunnel	size/Å
α	(1 × 1), (2 × 2)	1.89, 4.6
β	(1 × 1)	1.89
γ	(1 × 1), (1 × 2)	1.89, 2.3
δ	interlayer distance	7.0

amorphous and crystalline samples of MnO2.[31] On the basis of cyclic voltammetric data, SC values were calculated. The SC values obtained for δ-MnO2 were in the range of 80−110 F g^{-1}, which was slightly smaller than the values found for amorphous samples. The SC values obtained for β-MnO2 (5 F g^{-1}), γ-MnO2 (30 F g^{-1}), and λ-MnO2 (70 F g^{-1}) were smaller than the values obtained for δ-MnO2.[31]

The present trend of research in many fields is to employ nanosize materials, which are expected to possess better properties than the micrometer-size materials. Studies on the capacitance properties of various crystallographic forms of MnO2 are scarce in the literature.[31] The intention of the present study is to prepare nanosize particles of α-, β-, γ-, δ-, and λ-MnO2 samples and to evaluate their properties with a special interest in supercapacitor behavior. A comparison of the SC values of the various structures of MnO2 is made, and appropriate explanations for the variation of SC values are provided.

2. Experimental Section

All chemicals were of analytical grade, and they were used without further purification. MnSO4·H2O, KMnO4, Na2SO4, sodium dodecyl sulfate (SDS), and cyclohexanewere purchased
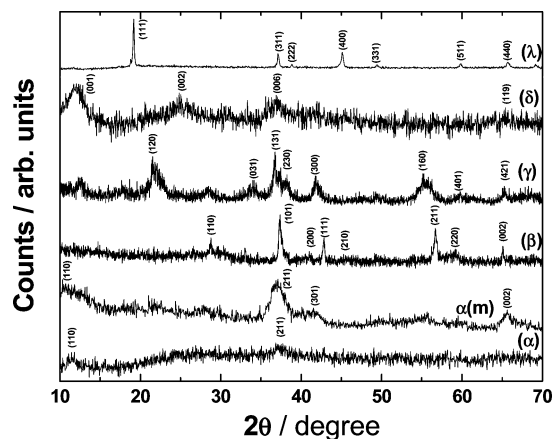

Figure 2. Powder XRD pattern of α-, α(m)-, β-, γ-, δ-, and λ- MnO2. The (*hkl*) planes are indicated. The data were recorded at a sweep rate of 0.5° min^{-1} using Cu Kα source.

**TABLE 2: Crystal Radius and Size of the Alkali Cation in Aqueous Solution[37]**

alkali cation	crystal radius/Å	in aqueous solution/Å
Li$^+$	0.6	6
Na$^+$	0.95	4
K$^+$	1.33	3
H$^+$		9

from Merck, n-butanol from SD Fine Chemicals, (NH4)2S2O8 from Ranbaxy, Mn(NO3)2·4H2O from Fluka, and LiMn2O4 from Aldrich. All solutions were prepared in doubly distilled (DD) water. Samples of MnO2 with different crystal structures were synthesized by the following procedures.

2.1. Synthesis of α-MnO2. Nanoparticles of α-MnO2 were synthesized by redox reaction between stoichiometric quantities of MnSO4 and KMnO4 in both aqueous medium[9] and a microemulsion medium.[15] In a typical synthesis in aqueous medium, 10 mL of 0.1 M KMnO4 solution was mixed with 10 mL of 0.15 M MnSO4·H2O solution and stirred continuously for 6 h. A dark-brown precipitate thus formed and was washed several times with DD water, centrifuged, and dried at 70 °C in air for 12 h. Details of the microemulsion method of synthesis of nanostructured MnO2 is reported elsewhere.[15] MnO2 samples obtained from aqueous and microemulsion routes are hereafter referred to as α-MnO2 and α-MnO2(m), respectively. About 300 mg of the product was synthesized in each batch.

2.2. Synthesis of β-MnO2. Nanorods of β-MnO2 were prepared by hydrothermal treatment of aqueous solution of Mn-(NO3)2·4H2O.[20] Twenty-five milliliters of 0.5 M Mn(NO3)2·4H2O solution was loaded into a Teflon-lined stainless-steel autoclave (capacity: 40 mL) and heated at 190 °C for 6 h. The autoclave was cooled slowly to room temperature. A dark brown powder was formed. It was washed several times with DD water, centrifuged, and dried at 70 °C in air for 12 h. Because the amount of product obtained in a batch of synthesis (typically 20 mg) was small, the synthesis was repeated several times to get sufficient quantity for the experiments. During this synthesis, it was noticed that a minor variation in temperature caused drastic variations in the properties of the product. After several experiments, the experimental conditions of hydrothermal synthesis were optimized.

2.3. Synthesis of γ-MnO2. Nanowires/nanorods of γ-MnO2 were prepared from MnSO4 using (NH4)2S2O8 as an oxidizing agent.[21] Stoichiometric amounts of MnSO4·H2O and (NH4)2S2O8 were dissolved in DD water. They were mixed together and heated at 80 °C for 4 h. A dark-brown precipitate was separated,
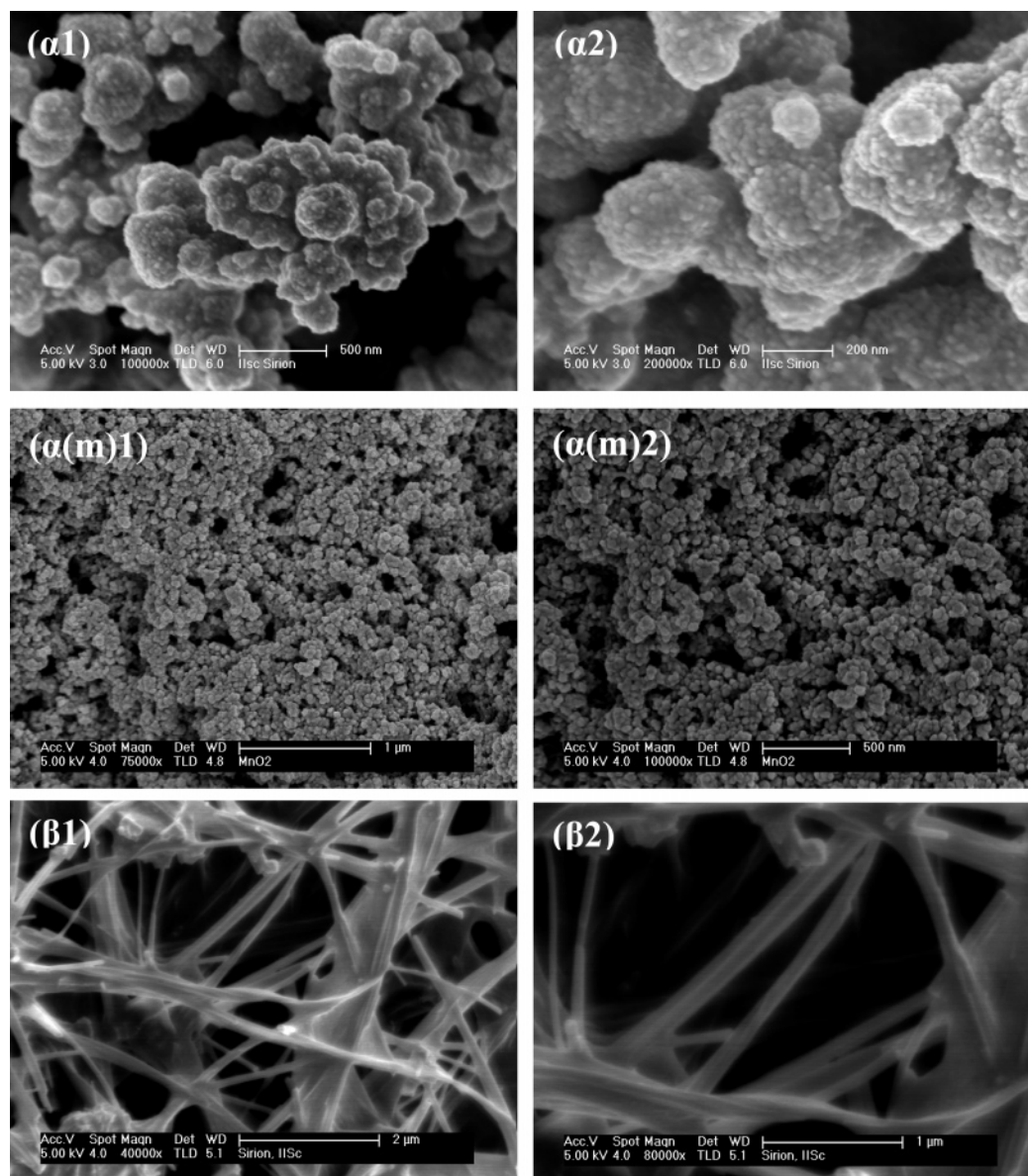
Figure 3. SEM micrographs of α-, α(m)-, and β-MnO₂. 1 and 2 refer to different magnifications of a sample.

washed, and dried at 70 °C. About 3.8 g of the product was synthesized in a batch.

2.4. Synthesis of δ-MnO₂. Nanoplatelets of δ-MnO₂ were prepared by following the same route of synthesis of α-MnO₂, but with double the stoichiometric amount of KMnO₄. The presence of excess K⁺ ion stabilizes the 2D layered δ-structure of MnO₂. The quantity obtained was about 340 mg.

**2.5. Synthesis of λ-MnO₂.** λ-MnO₂ was prepared by delithiation of LiMn₂O₄.[32] Spinel LiMn₂O₄ powder was treated with 0.5 M HCl at 25 °C for 24 h. About 500 mg of the product was obtained in a batch.

2.6. Characterization. Powder X-ray diffraction (PXRD) patterns of MnO₂ were recorded using Philips XRD X'PERT PRO diffractometer using Cu Kα radiation ($\lambda = 1.54178$ Å) as the source. The morphology of MnO₂ was examined using an FEI scanning electron microscope (SEM) model SIRION and an FEI high-resolution transmission electron microscope (HR-TEM) model TECNAI F 30. The Brunauer−Emmett−Teller (BET) surface area and pore volume were measured by the nitrogen gas adsorption−desorption method at 77 K using a Quantachrome surface area analyzer model Nova-1000. The pore size distribution was calculated by the Barrett−Jayner−

Halenda (BJH) method using the desorption branch of the isotherm. Samples were heated at 120 °C for 2 h in air prior to surface property measurements. IR spectra were recorded using a Perkin-Elmer FT-IR spectrophotometer model Spectrum One, using KBr pellets. KBr and samples were heated at 80 °C in vacuum overnight prior to measurements. Thermogravimetric analysis (TGA) was performed in the temperature range from ambient to 800 °C in air at a heating rate of 10 °C/min using a Perkin-Elmer thermal analyzer model Pyris Diamond TG/DTA.

2.7. Electrochemical Measurements. Electrodes were prepared on high-purity battery-grade Ni foil (0.18 mm thick) as the current collector. The Ni foil was polished with successive grades of emery, cleaned with detergent, washed copiously with DD water, rinsed with acetone, dried, and weighed. MnO₂ (70 wt %), acetylene black (20 wt %), and polyvinylidene difluoride (10 wt %) were ground in a mortar, and a few drops of 1-methyl-2-pyrrolidinone was added to form a syrup. It was coated on to the pretreated Ni foil (area of coating: 2 cm²) and dried at 110 °C under vacuum. Coating and drying steps were repeated to get the loading level of the active material close to 0.5 mg cm⁻². Finally, the electrodes were dried at 110 °C under vacuum for 12 h. A Sartorious balance model CP22D-OCE with 10 μg
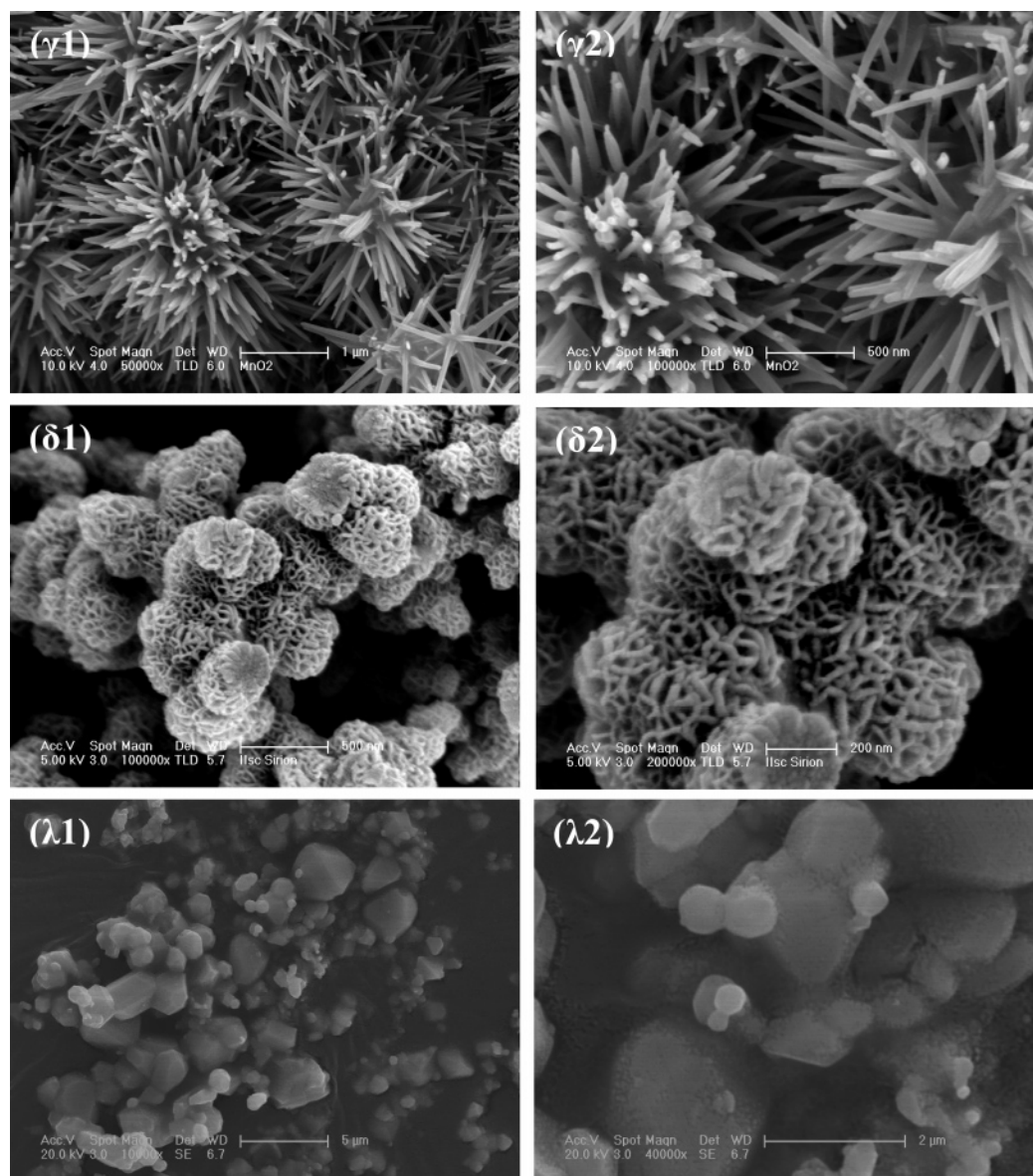
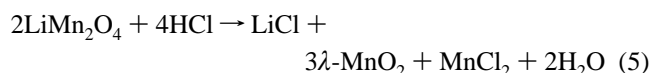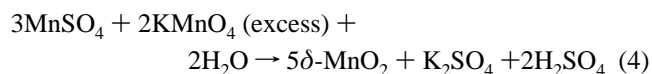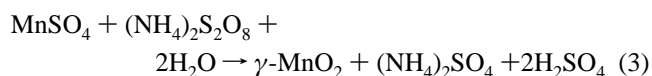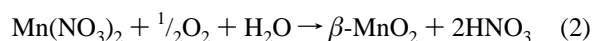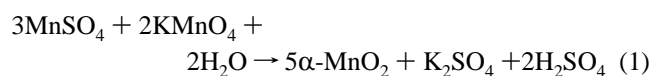**Figure 4.** SEM micrographs of γ-, δ-, and λ-MnO$_2$. 1 and 2 refer to different magnifications of a sample.

sensitivity was used for weighing the electrodes. A glass cell of capacity 70 mL, which had provisions for introducing a MnO$_2$ working electrode, Pt auxiliary electrodes, and a reference electrode, was employed for electrochemical studies. An aqueous solution of 0.1 M Na$_2$SO$_4$ was used as the electrolyte. A saturated calomel electrode (SCE) was used as the reference electrode, and potential values are reported against SCE. Electrochemical studies were carried out using a potentiostat–galvanostat EG&G model Versastat II or Solartron model SI 1287. All electrochemical experiments were carried out at 20 $\pm$ 2 °C.

3. Results and Discussion

The reactions involved in the synthesis of different crystallographic forms of MnO$_2$ are listed below:

$$3MnSO_4 + 2KMnO_4 + 2H_2O \rightarrow 5\alpha\text{-}MnO_2 + K_2SO_4 + 2H_2SO_4 \quad (1)$$

$$Mn(NO_3)_2 + {}^1/{}_2O_2 + H_2O \rightarrow \beta\text{-}MnO_2 + 2HNO_3 \quad (2)$$

$$MnSO_4 + (NH_4)_2S_2O_8 + 2H_2O \rightarrow \gamma\text{-}MnO_2 + (NH_4)_2SO_4 + 2H_2SO_4 \quad (3)$$

$$3MnSO_4 + 2KMnO_4 \text{ (excess)} + 2H_2O \rightarrow 5\delta\text{-}MnO_2 + K_2SO_4 + 2H_2SO_4 \quad (4)$$

$$2LiMn_2O_4 + 4HCl \rightarrow LiCl + 3\lambda\text{-}MnO_2 + MnCl_2 + 2H_2O \quad (5)$$

We have shown recently that α-MnO$_2$ prepared in a microemulsion medium (α-MnO$_2$(m)) possesses electrochemical properties superior to those of the samples prepared in aqueous medium.[15] Some important results of α-MnO$_2$(m) are also included here for the purpose of comparison.

3.1. XRD Studies. The structural frame work of MnO$_2$ consists of basic MnO$_6$ octahedra units, which are linked in different ways to produce different crystallographic forms.[22] The different ways of sharing the vertices and edges of MnO$_6$ octahedra units lead to the building of 1D, 2D, and 3D tunnel structures.[33] The different crystallographic forms are described by the size of the tunnel formed with the number of octahedra
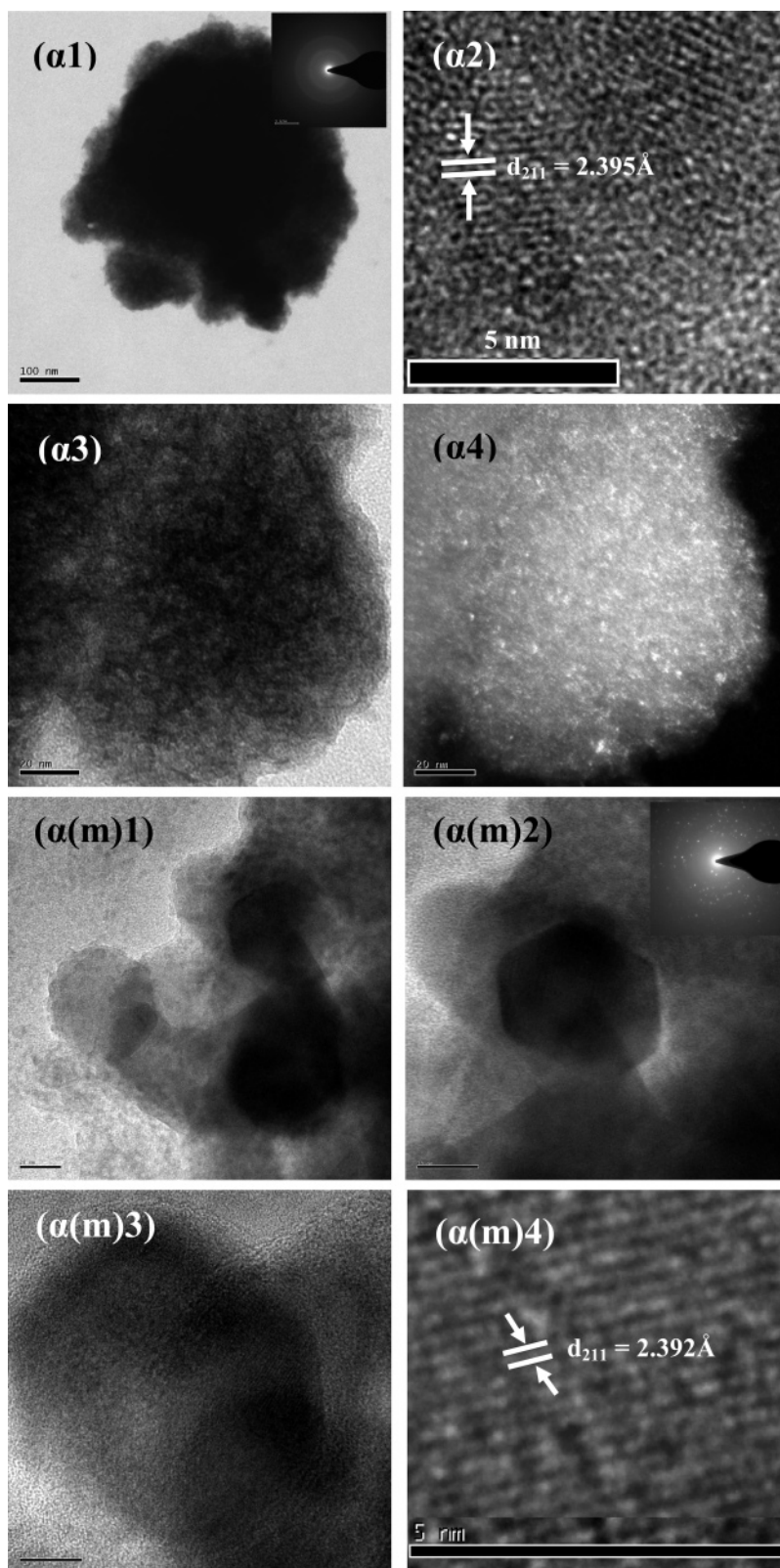
Figure 5. TEM image (α1), HRTEM image (α2), and bright-field (α3) and dark-field (α4) TEM image of α-MnO₂. SAD pattern is given as an inset in α1. Also shown are TEM images at different magnifications (α(m)1, α(m)2, and α(m)3), HRTEM image (α(m)4) of α-MnO₂(m). SAD pattern is given as an inset in α(m)2.

subunits ($n \times m$). The structures are shown schematically in Figure 1, and the type of tunnel formed as well as the size of tunnels are presented in Table 1.[34−36] The structure of α-MnO₂ (Figure 1α) consists of double chains of edge-sharing MnO_6 octahedra, which are linked at corners to form 1D (2×2) and (1×1) tunnels that extend in a direction parallel to the c axis

of the tetragonal unit cell. The size of the (2×2) tunnel is ~4.6 Å, which is suitable for insertion/extraction of alkali cations (Table 2).[34,37] A small amount of cations such as Li⁺, Na⁺, K⁺, NH₄⁺, Ba²⁺, or H₃O⁺ is required to stabilize the (2×2) tunnels in the formation of α-MnO₂.[34] β-MnO₂ (Figure 1β) is composed of single strands of edge-sharing MnO_6
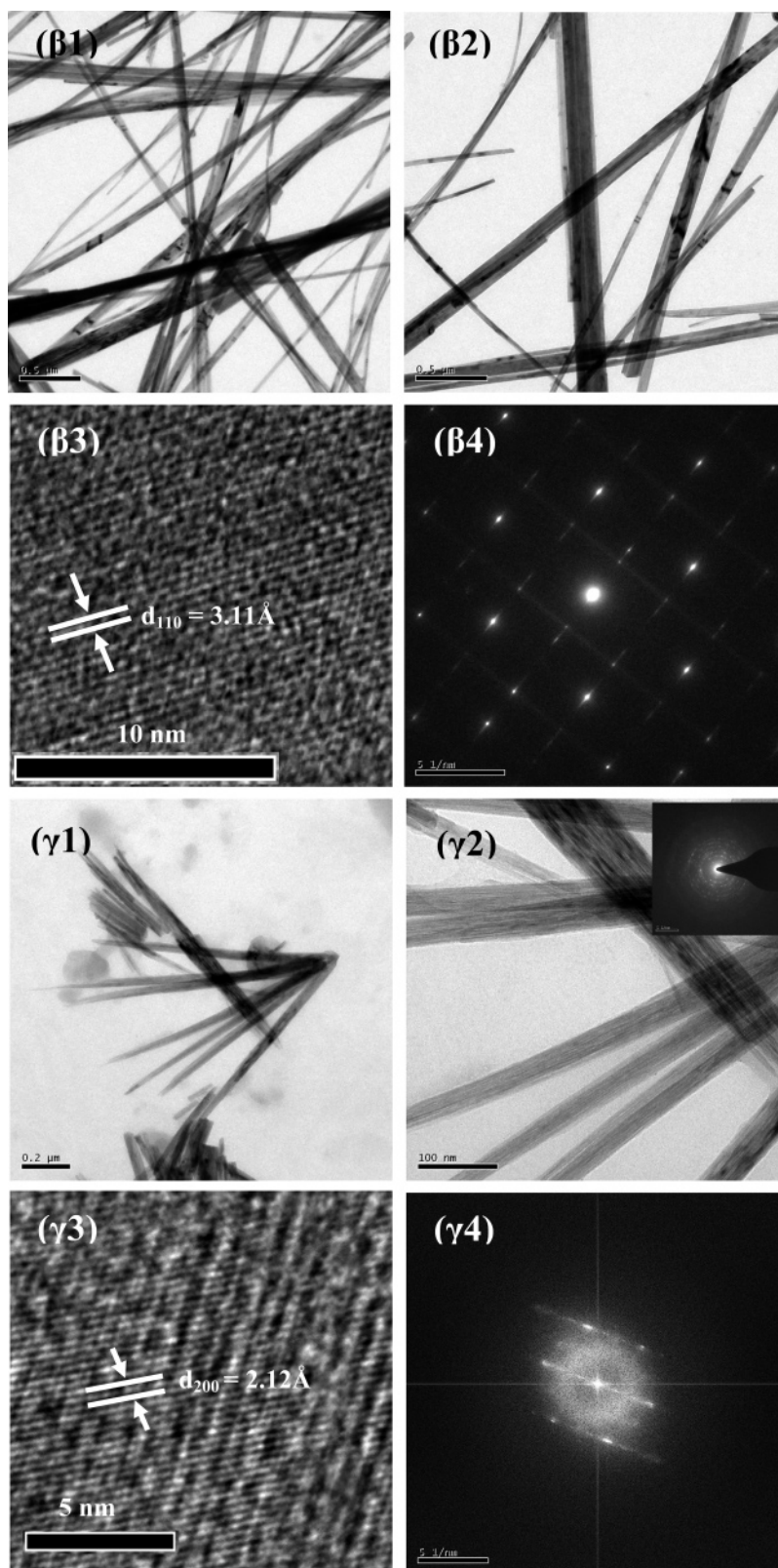
Figure 6. TEM images (β1, β2), HRTEM image of a single nanorod (β3), and the corresponding FFT pattern (β4) of β-MnO$_2$. Also shown are TEM images at different magnifications (γ1, γ2), HRTEM image (γ3), and the corresponding FFT pattern (γ4) of γ-MnO$_2$. SAD pattern is given as an inset in γ2.

octahedra to form a 1D (1 × 1) tunnel. Because of the narrow (1 × 1) tunnel of size (~1.89 Å),[35] β-MnO$_2$ cannot accommodate cations.[22] The structure of γ-MnO$_2$ (Figure 1γ) is random intergrowth of ramsdellite (1 × 2) and pyrolusite (1 × 1) domains.[38] This intergrowth structure can be described in terms of De Wolff disorder and microtwinning.[38] δ-MnO$_2$

(Figure 1δ) is a 2D layered structure with an interlayer separation of ~7 Å.[36] It has a significant amount of water and stabilizing cations such as Na$^+$ or K$^+$ between the sheets of MnO$_6$ octahedra. λ-MnO$_2$ (Figure 1λ) is a 3D spinel structure.[32]

Powder XRD patterns of MnO$_2$ samples are shown in Figure 2. Although the pattern of samples marked α and α(m) exhibit

fluorescence, broad peaks at $2\theta = 11.6$ and $37.3°$ for α and at $2\theta = 10.8$, 37.0, 41.7, and $65.5°$ for $\alpha(m)$ are clearly present. It is thus inferred that these samples are in a poorly crystalline state with a short-range α-crystallographic form (JCPDS no. 44-0141). The XRD patterns marked β and γ (Figure 2) confirm the formation of β- (JCPDS no. 24-0735) and γ- (JCPDS no. 14-0644) crystallographic forms of MnO_2, respectively. Broad peaks at $2\theta = 12.2$, 24.8, 37.0, and $65.4°$ in the pattern marked δ (Figure 2) correspond to δ-MnO_2 (JCPDS no. 18-0802), and it is also considered to be in a poorly crystalline phase. Unlike the above patterns, the diffraction pattern marked λ in Figure 2 consists of clear peaks, suggesting that this sample possesses a long-range crystalline order. This pattern was indexed to cubic symmetry with space group $Fd3m$ (no. 227) using the Appleman program, and the lattice constants were calculated. The lattice constants obtained are $a = b = c = 8.03$ Å, and these values are in good agreement with the reported data for the pure phase of λ-MnO_2 (JCPDS no. 44-0992).[32]

3.2. SEM and TEM Studies. SEM images of α-MnO_2, α-$MnO_2(m)$, and β-MnO_2 (two magnifications for each) are shown in Figure 3. α-MnO_2 and α-$MnO_2(m)$ are composed of spherical aggregates of nanoparticles without clear interparticle boundaries (Figure 3α1, α2, $\alpha(m)$1, and $\alpha(m)$2). Hydrothermal treatment of the aqueous $Mn(NO_3)_2$ solution yields 1D nanorods of β-MnO_2 (Figure 3β1 and β2), which are about 50 nm in diameter and several micrometers in length. Adjacent nanorods are fused to each other.

SEM images of γ-, δ-, and λ-MnO_2 are presented in Figure 4 in two magnifications for each. The morphology of γ-MnO_2 consists of spherical brushes with straight and radially grown nanorods. Several nanorods of $30-50$ nm in diameter and a few micrometers in length assemble together to form spherical brushes. δ-MnO_2 (Figure 4) consists of spherical agglomerates made of interlocked short fibers of $\sim 10-20$ nm in diameter. The particles of λ-MnO_2 (Figure 4) exhibit random shapes with sizes varying from a few tens of nanometers to a few micrometers.

TEM images of α-MnO_2 and α-$MnO_2(m)$ are presented in Figure 5. The TEM image (Figure 5α1) shows that α-MnO_2 consists of agglomerated particles. A selected area diffraction (SAD) pattern is shown in the inset of Figure 5α1. It is seen that a couple of weak rings corresponding to the crystal planes of α-MnO_2 are evolved, indicating the poor crystalline nature of the sample. The HRTEM image (Figure 5α2) indicates the crystalline nature of the sample. The bright-field and corresponding dark-field TEM images of α-MnO_2 (Figure 5α3 and α4) suggest that several nanoparticles of less than 5 nm are agglomerated.

It seen in Figure 5$\alpha(m)$1, $\alpha(m)$2, and $\alpha(m)$3 that α-MnO_2-(m) has a hexagonal shape of $\sim$50 nm size. The SAD pattern is shown as the inset to Figure 5$\alpha(m)$2. It is seen that rings corresponding to crystal planes are absent. The spotty diffraction pattern suggests that the nanoparticles of MnO_2 obtained from microemulsion route possess single-crystal character. The HR-TEM image (Figure 5$\alpha(m)$4) shows the interplanar distance to be 2.392 Å, which agrees well with separation between the [211] planes of α-MnO_2.

Shown in Figure 6β1 and β2 are nanorods of β-MnO_2, which are $20-50$ nm in diameter and several micrometers in length. In the HRTEM (Figure 6β3), lattice fringes are clearly seen. The interplanar distance is 0.311 nm, which agrees well with the separation between the [110] planes of β-MnO_2. The corresponding FFT pattern (Figure 6β4) displays spot lines perpendicular to the lattice fringes of Figure 6β3, suggesting

TABLE 3: Specific Surface Area and Total Pore Volume of Polymorphic MnO_2

crystallographic form	specific surface area $(m^2\,g^{-1})$	total pore volume $(cc/Å/g)$	average pore diameter (Å)
α	17.29	0.03675	85.020
$\alpha(m)$	123.39	0.24811	80.431
γ	31.56	0.06006	76.112
δ	20.93	0.06750	129.014
λ	5.21	0.00878	67.451

the crystalline nature of β-MnO_2. Furthermore, the length of the nanorod extends along the [110] direction.

The TEM images shown in Figure 6γ1 and γ2 suggest that nanorods of γ-MnO_2 grow in a random fashion. The SAD pattern shown as inset in Figure 6γ2 reveals that rings and spots corresponding to crystal planes of γ-MnO_2 are better evolved compared to α-MnO_2, which is in agreement with the XRD results (Figure 2). It is seen in the HRTEM image (Figure 6γ3) that several nanowires of less than 1 nm are self-assembled to form nanorods. The interplanar distance calculated from the lattice fringes of HRTEM is 0.212 nm, which corresponds to separation of the [200] plane. Lattice fringes are inclined at about 60° toward the self-assembled nanowires. It is also seen in the HRTEM that nanorods exhibit better crystalline character at the center of the rod than the outer part. The FFT pattern (Figure 6γ4) corresponding to the HRTEM image of γ-MnO_2 shows spot lines perpendicular to lattice fringes confirming the crystalline nature and also indicating that the nanorod extends in the [200] direction.

TEM images of δ-MnO_2 (Figure 7 δ1, δ2, and δ3) show that nanofibers with thicknesses less than 10 nm are agglomerated to form interconnected spherical structures of δ-MnO_2. The SAD pattern shown as inset in Figure 7δ1 supports the partial crystalline nature of δ-MnO_2 inferred from the powder XRD pattern. The HRTEM image (Figure 7δ4) indicates the crystalline nature of the sample.

TEM images of λ-MnO_2 (Figure 7λ1 and λ2) suggest that the particles grow in different shapes and the adjacent particles fuse to each other. Spots evolved in the FFT pattern (Figure 7λ3) are indexed, and they confirm the highly crystalline nature of λ-MnO_2. Energy-dispersive analysis of the X-ray (EDAX) spectrum shown in Figure 7λ4 indicates the presence of manganese and oxygen.

3.3. Porosity Measurements. Nitrogen adsorption−desorption isotherms for MnO_2 samples were measured (see Supporting Information, Figure S1). The isotherms of α-, $\alpha(m)$-, γ-, and δ-MnO_2 belong to type IV, which indicates the mesoporous nature of the samples with an hysteresis loop. Alternatively, the isotherm of λ-MnO_2 belongs to type II, which is a characteristic feature of nonporous solids.[39] The specific surface area, total pore volume, and average pore diameter for all crystallographic forms of MnO_2 are listed in Table 3. Although α-MnO_2 and α-$MnO_2(m)$ exhibit the same type of adsorption−desorption isotherm, their surface area and pore size distribution are different. The specific surface area of 123 $m^2\,g^{-1}$ and total pore volume of 0.25 $cm^3\,Å^{-1}\,g^{-1}$ obtained for α-$MnO_2(m)$ are greater than the specific surface area of 17.3 $m^2\,g^{-1}$ and pore volume of 0.037 $cm^3\,Å^{-1}\,g^{-1}$ obtained for α-MnO_2. These differences indicate that α-$MnO_2(m)$ is more porous than α-MnO_2, and, hence, it is anticipated that α-$MnO_2(m)$ possesses higher electrochemical activity.

Lower values of specific surface area and total pore volume are observed for γ-MnO_2 compared to α-$MnO_2(m)$. A high average pore diameter of 129 Å obtained for δ-MnO_2 is
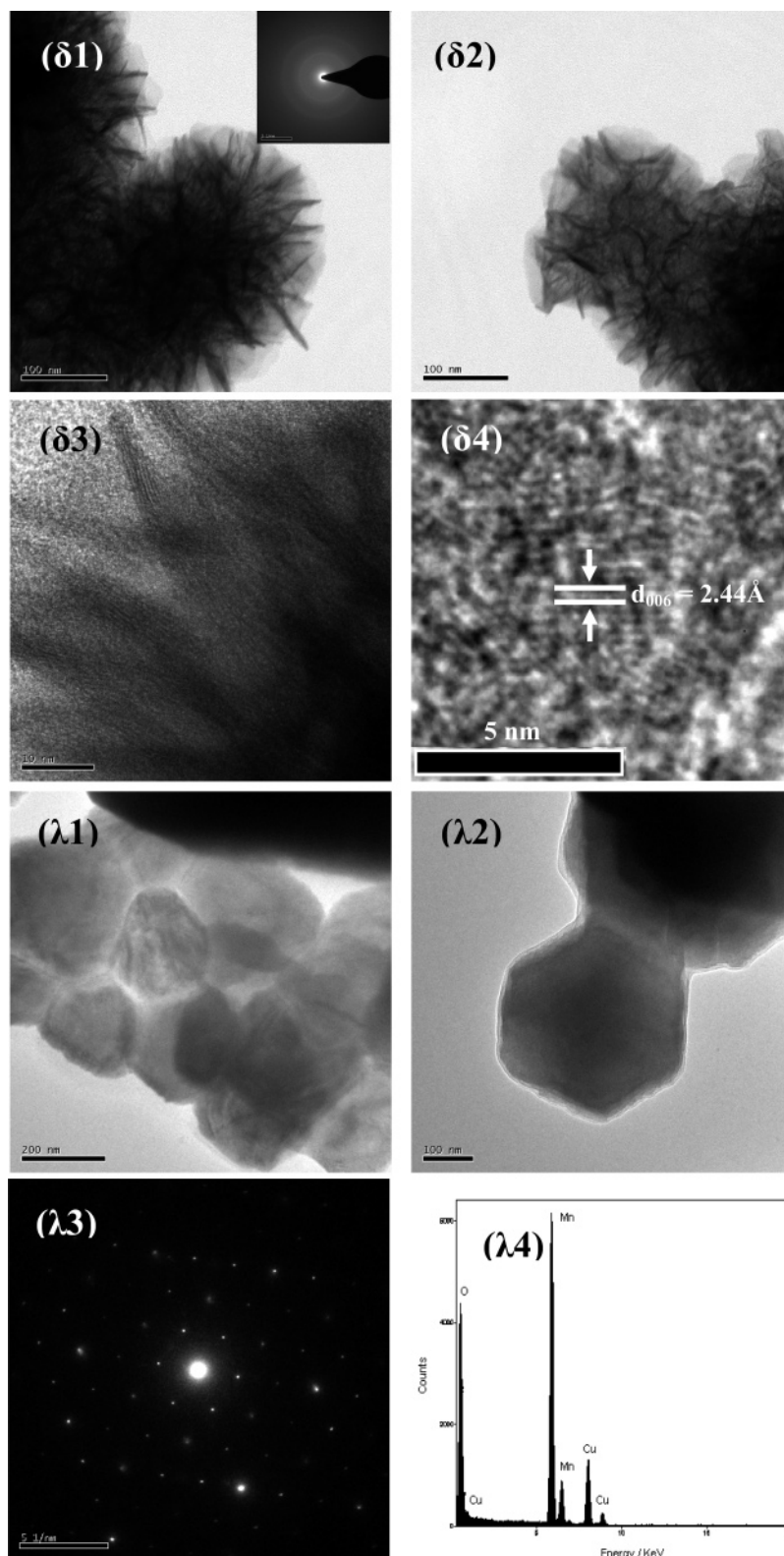
Figure 7. TEM images at different magnifications (δ1, δ2, and δ3) and HRTEM image (δ4) of δ-MnO$_2$. SAD pattern in given as an inset in δ1. Also shown are TEM images at different magnifications (λ1, λ2), FFT pattern (λ3), and EDAX spectrum (λ4) of λ-MnO$_2$.

attributed to the wide interlayer separation. The lowest values of specific surface area (5.2 m^2 g^{-1}) and total pore volume (0.0088 cm^3 Å^{-1} g^{-1}) are obtained for λ-MnO$_2$. It is inferred from the adsorption isotherm and Table 3 that λ-MnO$_2$ is the least porous among all samples.

3.4. Vibrational Spectroscopic Studies. In IR spectra of MnO$_2$ samples (see Supporting Information, Figure S2), a broad band around 400−700 cm^{-1} observed for all crystallographic

forms of MnO$_2$ is ascribed to Mn−O bending vibration. A broad band around 3400 cm^{-1} and a weak band around 1630 cm^{-1} observed for α-, α(m)-, γ-, and δ-MnO$_2$ are attributed to stretching and bending vibrations of H−O−H, respectively.[40] Bands corresponding to vibrations of water molecules are not observed for β- and λ-MnO$_2$, suggesting that these phases do not contain water. This is in agreement with the literature report that β- and λ-MnO$_2$ do not contain lattice water.[22,32]

3.5. Thermogravimetric Analysis. TGA thermograms of different crystallographic forms of MnO_2 were recorded (see Supporting Information, Figure S3). Progressive weight loss from room temperature to 500 °C is observed for α-, α(m)-, γ-, and δ-MnO_2 samples. This is due to removal of water.[13] Weight loss is not observed in the case of β- and λ-MnO_2 samples because of the absence of water in these phases.[22,32] At around 550 °C, a sudden weight loss is observed for all samples except for δ-MnO_2. This weight loss corresponds to the transformation of MnO_2 to Mn_2O_3.[41] As δ-MnO_2 prepared in the presence of excess of K^+ ions, these ions present between the layers of δ-MnO_2 prevent the conversion of MnO_2 to Mn_2O_3. The weight loss corresponding to this process is sharp in the case of β-MnO_2 as it has very narrow (1×1) tunnel in which no stabilizing ions are present.[22] The weight loss is much less (<2 wt %) in the case of α-MnO_2 because the stabilizing cations present at low concentration in its (2×2) tunnels prevent the transformation to a large extent. Weight loss values of about 2 and 6 wt % are observed for α- and α-MnO_2(m), respectively. This difference is ascribed to different amounts of K^+ ions present in their (2×2) tunnels. All crystallographic forms of MnO_2 were annealed in air for 3 h at various temperatures ranging from ambient to 800 °C at intervals of 200 °C, and powder XRD patterns were recorded (not shown). Conversion of MnO_2 to Mn_2O_3 is observed for all samples annealed at ≥400 °C except for δ-MnO_2, thus supporting the analysis of TGA data.

3.6. Electrochemical Studies. There are two mechanisms proposed for charge storage in MnO_2. The first mechanism involves intercalation/extraction of protons (H_3O^+) or alkali cations such as Li^+, Na^+, K^+, and so forth into the bulk of oxide particles with concomitant reduction/oxidation of the Mn ion.[10,23]

$$MnO_2 + M^+ + e^- \rightleftharpoons MnOOM \ (M^+ =$$
$$Li^+, Na^+, K^+, or \ H_3O^+) \ (6)$$
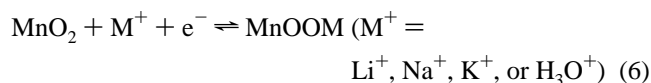
The second mechanism is a surface process, which involves the adsorption/desorption of alkali cations.[17]

$$(MnO_2)_{surface} + M^+ +$$
$$e^- \rightleftharpoons (MnOOM)_{surface} \ (M^+ = Li^+, Na^+, K^+, or \ H_3O^+) \ (7)$$
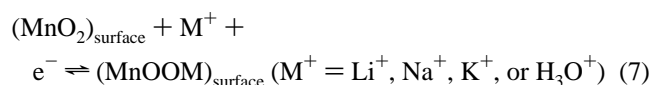
Although the bulk process (reaction 6) is anticipated to occur in crystalline samples of MnO_2, the surface process (reaction 7) occurs in amorphous samples.[24]

Electrodes, which were fabricated with different crystallographic forms of MnO_2, were subjected to electrochemical studies in aqueous 0.1 M Na_2SO_4 electrolyte. Cyclic voltammograms recorded between 0 and 1.0 V at a sweep rate of 20 mV s^{-1} for all electrodes are shown in Figure 8. All voltammograms are nearly rectangular in shape. The rectangular shape of the voltammogram is a fingerprint for capacitance behavior.[1-3] Among all samples, the highest current density is obtained for α-MnO_2(m) (Figure 8), which is attributed to the higher porosity and greater surface area in relation to the rest of the samples. The voltammograms of α- and δ-MnO_2 electrodes nearly overlap, suggesting that the SC values of α- and δ-MnO_2 are comparable. The voltammetric current of the γ-MnO_2 electrode (Figure 8) is lower than the currents of the α-, α(m)-, and δ-MnO_2 electrodes. There is an increase in current near 0 and also at 1 V, suggesting that the overpotentials for the hydrogen evolution reaction (HER) as well as the oxygen evolution reaction (OER) are lower for γ-MnO_2. The current values
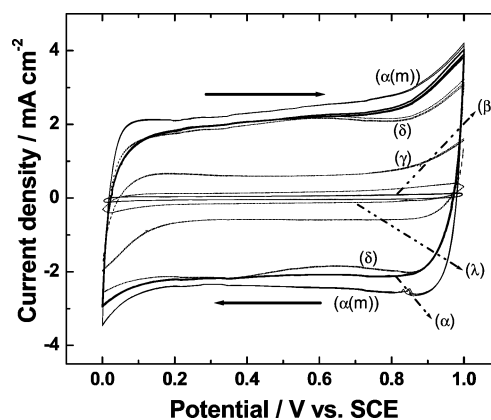
Figure 8. Cyclic voltammograms of α-, α(m)-, β-, γ-, δ-, and λ- MnO_2 recorded between 0 and 1.0 V vs SCE in aqueous 0.1 M Na_2SO_4 at a sweep rate of 20 mV s^{-1}.

(Figure 8) for the β- and λ-MnO_2 electrodes are very low, suggesting that the capacitance values of these samples are very small. Thus, the SC values of MnO_2 samples qualitatively decrease in the following order: α(m) > α ≅ δ > γ > λ > β. Quantitatively, the SC values were evaluated from galvanostatic charge−discharge cycling as described below.

The electrodes were subjected to galvanostatic charge−discharge cycling between 0 and 1.0 V in aqueous 0.1 M Na_2SO_4 electrolyte at several current densities. The variations of potential with time during the first few charge−discharge cycles at a current density of 0.5 mA cm^{-2} are shown in Figure 9. Linear variation of potential during both charging and discharging processes are observed for all MnO_2 electrodes. The linear variation of potential during charging and discharging processes is another criterion for capacitance behavior of a material in addition to exhibiting rectangular voltammograms.[1] The durations of charging and discharging are almost equal for each electrode, implying high columbic efficiency of charge−discharge cycling. However, the durations of charge and discharge cycles are different for different crystallographic forms of MnO_2, suggesting that the SC values are different similar to the observation made from cyclic voltammograms (Figure 8). The SC values were calculated from charge−discharge cycles using the following equation

$$SC = It/(\Delta Em) \quad (8)$$

where, I is the discharge (or charge) current, t is the discharge (or charge) time, ΔE (=1.0 V) is the potential window of cycling, and m is the mass of MnO_2. The discharge SC values for all electrodes are presented in Figure 10. The variation of SC values follows the order α(m) > α ≅ δ > γ > λ > β. The SC values are 240 F g^{-1} for α-MnO_2 and 236 F g^{-1} for δ-MnO_2. Alternatively, they are as low as 9 F g^{-1} for β-MnO_2 and 21 F g^{-1} for λ-MnO_2. The SC values are generally expected to follow the trend of surface area if capacitance is due to double-layer charging or adsorption of cations on the surface of active material. In recent studies, it is shown that the surface process is dominant in the amorphous sample of MnO_2.[24] Because all samples of MnO_2 prepared in the present study are in the crystalline or poorly crystalline state of various structures, the low values of SC obtained are not due to the amorphous nature of the samples. In fact, λ-MnO_2 has greater crystallinity than the rest of the samples (Figure 2) because of its larger particle size (Figure 4), but its SC is low. It is inferred that SC values largely depend on crystal structure and not on surface area while making comparisons among various structures (within the same
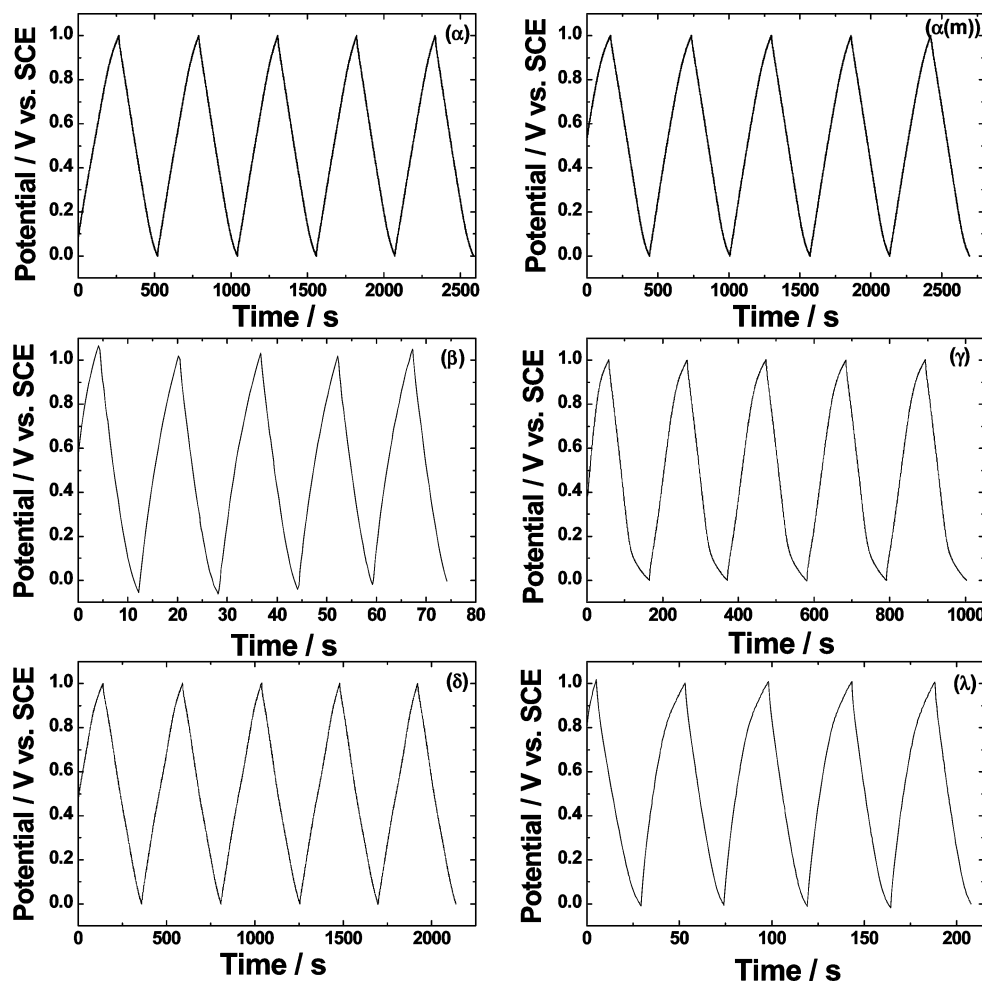
Figure 9. Charge−discharge cycles of α-, α(m)-, β-, γ-, δ-, and λ- MnO$_2$ at a c.d. of 0.5 mA cm^{-2} in 0.1 M Na$_2$SO$_4$.
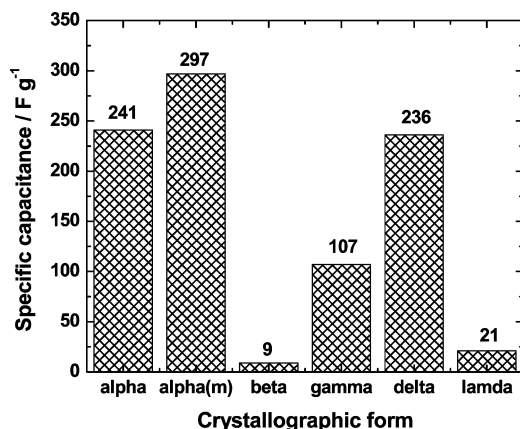
Figure 10. Specific capacitance of α-, α(m)-, β-, γ-, δ-, and λ- MnO$_2$ electrodes in 0.1 M Na$_2$SO$_4$ at a c.d. of 0.5 mA cm^{-2} between 0 and 1.0 V vs SCE.

structure, surface area influences to some extent as explained later for α-MnO$_2$ and α-MnO$_2$(m)). For instance, the surface area of γ-MnO$_2$ is greater than that of either α-MnO$_2$ or δ-MnO$_2$ (Table 3). But, the SC of γ-MnO$_2$ is less than that of either α- or δ-MnO$_2$ samples (Figure 10). As explained below, the supercapacitance of MnO$_2$ is mainly due to insertion/extraction of alkali cations into/from MnO$_2$ (reaction 6), if the crystal structure can accommodate these ions in its bulk. The surface process (reaction 7) is not important in such crystal structures in exhibiting large values of capacitance. If the structure does not possess a sufficient gap to accommodate cations, then low

values of capacitance are obtained. The capacitance in such structures is only due to the surface adsorption (reaction 7).

Although the explanations given below reveal that the crystal structure greatly influences the SC of MnO$_2$, it is inferred from the results (Figure 10) that within a given crystal structure the other physical factors such surface area, porosity, and so forth influence the SC values. This aspect is evident from the SC values of α-MnO$_2$ and α-MnO$_2$(m). The SC is 297 F g^{-1} for α-MnO$_2$(m) against 240 F g^{-1} for α-MnO$_2$. The higher SC (by about ∼24%) is attributed to the greater surface area and higher porosity of α-MnO$_2$(m) in relation to α-MnO$_2$ (Table 3). These properties of α-MnO$_2$(m) facilitate higher efficiency of utilization of the particles in the electrode, which leads to greater SC in comparison with the α-MnO$_2$ electrode.

As stated previously, α-MnO$_2$ has 1D structure with (2 × 2) and (1 × 1) tunnels, whereas δ-MnO$_2$ has a 2D layered structure (Figure 1). Alkali cations or protons (Table 2) can be intercalated into the wide (2 × 2) tunnels (∼4.6 Å) of α-MnO$_2$[34] and in between the layers (∼7 Å) of 2D δ-MnO$_2$.[36] The comparable SC values (Figure 10) of α- and δ-MnO$_2$ are attributed to similarity in the amount of insertion/extraction of alkali cations into the tunnels of α-MnO$_2$ and between the layers of δ-MnO$_2$. Because γ-MnO$_2$ has moderate (1 × 2) and narrow (1 × 1) size tunnels, the amount of alkali cations inserted into tunnels of γ-MnO$_2$ is less than that of ions inserted into α-MnO$_2$ as well as δ-MnO$_2$. Alkali cations or protons cannot undergo insertion into narrow (1 × 1) tunnels because the size of the tunnel is smaller than that of alkali cations or protons (Tables 1 and 2).[22] Alternatively, the (1 × 2) tunnel γ-MnO$_2$ can

Figure 11. Dependence of specific capacitance on current density of charge−discharge cycling of α-, $\alpha(m)$-, β-, γ-, δ-, and λ- MnO$_2$ electrodes in 0.1 M Na$_2$SO$_4$ between 0 and 1.0 V vs SCE.


Figure 12. Cycle-life data of α-, $\alpha(m)$-, β-, γ-, δ-, and λ- MnO$_2$ electrodes in 0.1 M Na$_2$SO$_4$ at a c.d. of 0.5 mA cm^{-2} between 0 and 1.0 V vs SCE.
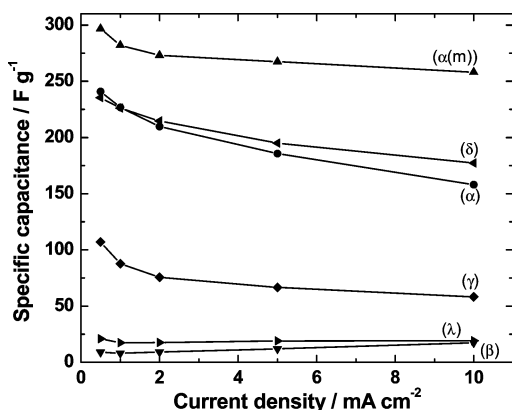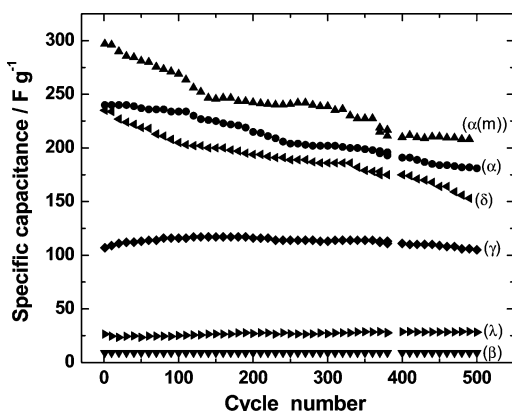
accommodate the ions. Hence, γ-MnO$_2$ has only about half of the specific capacitance of α- and δ-MnO$_2$. Because β-MnO$_2$ has only narrow (1 × 1) tunnels, cations cannot be inserted into it.[22] The observed specific capacitance of 9 F g^{-1} for β-MnO$_2$ and 21 F g^{-1} for λ-MnO$_2$ could be attributed to the double-layer charging and adsorption of ions.

The variation of SC of the MnO$_2$ electrodes with an increase in current density (c.d.) is shown in Figure 11. A decrease in SC with an increase in c.d. is observed for all crystallographic forms, which is due to a decrease in the efficiency of utilization of the active materials at high c.d. values. Similar to these results, a fade of SC with increased cyclic voltammetric sweep rate was reported.[31] It was inferred that not only surface reactions contribute to the charge storage mechanism in MnO$_2$ but surface and bulk faradaic reactions are also involved. There is a decrease in SC about 34% when the c.d. is increased from 0.5 to 10 mA cm^{-2} for α-MnO$_2$. However, this decrease is only about 13% for α-MnO$_2$(m). The superior rate capability of α-MnO$_2$(m) is again attributed to higher surface area and higher porosity, which leads to a higher rate of insertion/extraction of cations in comparison with α-MnO$_2$.

3.7. Cycle-Life Test. Electrodes made of all crystallographic forms of MnO$_2$ were subjected to extended charge−discharge cycling at a c.d. of 0.5 mA cm^{-2}, and the variation of SC as a function of cycle number is shown in Figure 12. The SC values of ∼240 F g^{-1} observed during the initial stages of cycling for α- and δ-MnO$_2$ decrease gradually, respectively, to 180 and 155 F g^{-1} at the end of 500 cycles (Figure 12). Similarly, there is a decrease in SC from ∼300 to 210 F g^{-1} at the end of 500 cycles for α-MnO$_2$(m). In the cases of β- and λ-MnO$_2$, SC is

invariant suggesting that their low values of capacitance are due to double-layer charging and physisorption of ions. The SC is nearly invariant in the range of 110−120 F g^{-1} for γ-MnO$_2$ on cycling. Almost all capacitor studies of MnO$_2$ reported in the literature involve only α-MnO$_2$ and a decrease in SC on cycling is reported widely.[9,15,24,42] In a recent study, the decrease in SC is attributed to the corrosion behavior of the substrate used for coating MnO$_2$.[42] In the present study, Ni foil is used for fabrication of all electrodes. Nevertheless, SC is invariant for the γ-MnO$_2$ electrode and it decreases for α-, α-(m)-, and δ-MnO$_2$ electrodes. This indicates that corrosion of the Ni substrate is not a significantly contributing factor in the present studies. Although the exact reasons for the stable capacity of γ-MnO$_2$ and the unstable capacity of α-, α(m)-, and δ-MnO$_2$ are not clearly understood, it is likely that the α and δ forms of MnO$_2$ undergo a gradual change in their crystallographic structures. Further experiments are needed in this direction.

4. Conclusions

Nanostructured MnO$_2$ samples with different crystal structures are synthesized, and they are investigated as electrode materials for electrochemical capacitors in aqueous 0.1 M Na$_2$SO$_4$ solution. The specific capacitance values decrease in the order of $\alpha(m) > \alpha \cong \delta > \gamma > \lambda > \beta$. The presence of narrow (1 × 1) tunnels in β-MnO$_2$ makes it unsuitable for capacitor application because it cannot accommodate cations during charge−discharge cycling. The high SC values obtained for layered δ-MnO$_2$ and α-MnO$_2$ are ascribed to their large interlayer separation (∼7 Å) and larger tunnel size (∼4.6 Å), respectively. The adsorption of cations (surface process, reaction 7) plays an important role in deciding the magnitude of specific capacitance not only in amorphous samples, as has been considered hitherto, but also in crystalline samples of MnO$_2$, which do not have sufficient gaps in their structures. Amazingly, γ-MnO$_2$, which is a preferred material for battery application, has only a moderate capacitance value.

Supporting Information Available: Nitrogen adsorption−desorption isotherms, IR spectra, and TGA thermograms of MnO$_2$. This material is available free of charge via the Internet at http://pubs.acs.org.

References and Notes

(1) Conway, B. E. *Electrochemical Supercapacitors, Scientific Fundamentals and Technological Applications;* Kluwer Academic/Plenum Press: New York, 1999; p 1.

(2) Conway, B. E. *J. Electrochem. Soc.* **1991**, *138*, 1539.

(3) Sarangapani, S.; Tilak, B. V.; Chen, C. P. *J. Electrochem. Soc.* **1996**, *143*, 3791.

(4) Burke, A. *J. Power Sources* **2000**, *91*, 37.

(5) Zheng, J. P.; Jow, T. R. *J. Electrochem. Soc.* **1995**, *142*, L6.

(6) Zheng, J. P.; Cygan, P. J.; Jow, T. R. *J. Electrochem. Soc.* **1995**, *142*, 2699.

(7) Zheng, J. P. *Electrochem. Solid-State Lett.* **1999**, *2*, 359.

(8) Santos, M. C.; Terezo, A. J.; Fernandes, V. C.; Pereira, E. C.; Bulhoes, L. O. S. *J. Solid State Electrochem.* **2005**, *9*, 91.

(9) Lee, H. Y.; Goodenough, J. B. *J. Solid State Chem.* **1999**, *144*, 220.

(10) Pang, S. C.; Anderson, M. A.; Chapman, T. W. *J. Electrochem. Soc.* **2000**, *147*, 444.

(11) Lee, H. Y.; Kim, S. W.; Lee, H. Y. *Electrochem. Solid-State Lett.* **2001**, *4*, A19.

(12) Toupin, M.; Brousse, T.; Belanger, D. *Chem. Mater.* **2002**, *14*, 3946.

(13) Jeong, Y. U.; Manthiram, A. *J. Electrochem. Soc.* **2002**, *149*, A1419.

(14) Devaraj, S.; Munichandraiah, N. *Electrochem. Solid-State Lett.* **2005**, *8*, A373.

(15) Devaraj, S.; Munichandraiah, N. *J. Electrochem. Soc.* **2007**, *154*, A80.

(16) Devaraj, S.; Munichandraiah, N. *J. Electrochem. Soc.* **2007**, *154*, A901.

(17) Toupin, M.; Brousse, T.; Belanger, D. *Chem. Mater.* **2004**, *16*, 3184.

(18) Subramanian, V.; Zhu, H.; Vajtai, R.; Ajayan, P. M.; Wei, B. *J. Phys. Chem. B* **2005**, *109*, 20207.

(19) Huang, X.; Yue, H.; Attia, A.; Yang, Y. *J. Electrochem. Soc.* **2007**, *154*, A26.

(20) Cheng, F.; Zhao, J.; Song, W.; Li, C.; Ma, H.; Chen, J.; Shen, P. *Inorg. Chem.* **2006**, *45*, 2038.

(21) Wang, X.; Li, Y. *Chem.—Eur. J.* **2003**, *9*, 300.

(22) Thackeray, M. M. *Prog. Solid State Chem.* **1997**, *25*, 1.

(23) Kuo, S. L.; Wu, N. L. *J. Electrochem. Soc.* **2006**, *153*, A1317.

(24) Ragupathy, P.; Vasan, H. N.; Munichandraiah, N. *J. Electrochem. Soc.* **2008**, *155*, A34.

(25) Bricker, O. *Am. Mineral.* **1965**, *50*, 1296.

(26) Shen, Y. F.; Zerger, R. P.; DeGuzman, R. N.; Suib, S. L.; McCurdy, L.; Potter, D. I.; O'Young, C. L. *Science* **1993**, *260*, 511.

(27) Wong, S. T.; Cheng, S. *Inorg. Chem.* **1992**, *31*, 1165.

(28) Hill, L. I.; Portal, R.; Verbaere, A.; Guyomard. D. *Electrochem. Solid-State Lett.* **2001**, *4*, A180.

(29) Hill, L. I.; Verbaere, A.; Guyomard. D. *J. Power Sources* **2003**, *119−121,* 226.

(30) Lin, H. Y.; Sun, Y. P; Weng, B. J; Yang, C. T; Suen, N. T; Liao, K. H; Huang, Y. C; Ho, J. Y; Chong, N. S; Tang, H. Y. *Electrochim. Acta* **2007**, *52*, 6548.

(31) Brousse, T.; Toupin, M.; Dugas, R.; Athouel, L.; Crosnier, O.; Belanger, D. *J. Electrochem. Soc.* **2006**, *153*, A2171.

(32) Hunter, J. C. *J. Solid State Chem.* **1981**, *39*, 142.

(33) Feng, Q.; Yanagisawa, K.; Yamasaki, N. *J. Porous Mater.* **1998**, *5*, 153.

(34) Brock, S. L; Duan, N; Tian, Z. R; Giraldo, O; Zhou, H; Suib, S. L. *Chem. Mater.* **1998**, *10*, 2619.

(35) Baur, W. H. *Acta Crystallogr.* **1976**, *B32,* 2200.

(36) Ma, R.; Bando, Y.; Zhang, L.; Sasaki, T. *Adv. Mater.* **2004**, *16*, 918.

(37) Reddy, R. N.; Reddy, R. G. *J. Power Sources* **2003**, *124*, 330.

(38) De Wolff, P. M. *Acta Crystallogr.* **1959**, *12*, 341.

(39) Gregg, S. J.; Sing, K. S. W. *Adsorption, Surface Area and Porosity;* Academic Press: London, 1982.

(40) Potter, R. M.; Rossman, G. R. *Am. Mineral.* **1979**, *64*, 1199.

(41) Tsang, C.; Kim, J.; Manthiram, A. *J. Solid State Chem.* **1998**, *137*, 28.

(42) Brousse, T.; Taberna, P. L.; Crosnier, O.; Dugas, R.; Guillemet, P.; Scudeller, Y.; Zhou, Y.; Favier, F.; Belanger, D.; Simon, P. *J. Power Sources* **2007**, *173*, 633.